CFD BASED ANALYSES OF THE EFFECTS OF 2017 NASCAR XFINITY RACING SERIES AERODYNAMIC RULE CHANGES

by

Nazarii Olkhovskyi

A thesis submitted to the faculty of
The University of North Carolina at Charlotte
in partial fulfillment of the requirements
for the degree of Master of Science in
Mechanical Engineering

Charlotte

2019

Approved by:

_____
Dr. Mesbah Uddin

_____
Dr. Jerre Hill

_____
Dr. Peter Tkacik

ABSTRACT

NAZARII OLKHOVSKYI. CFD Based Analyses of the Effects of 2017 NASCAR Xfinity Racing Series Aerodynamic Rule Changes. (Under the direction of DR. MESBAH UDDIN)

Xfinity racing series is an American stock car racing series organized by NASCAR. For the 2017 racing season, NASCAR introduced new regulations for this series in order to decrease aerodynamic influence on vehicle performance. Using only open-source Computational Fluid Dynamics (CFD) tools this work describes the differences in the aerodynamic performance between the 2016 and 2017 TOYOTA Camry Xfinity race-cars. During the CFD validation process, it was observed that none of the standard turbulence models, with default turbulence model closure coefficients, were able to provide the race-car aerodynamic characteristics prediction with an acceptable accuracy as compared to experiments, and that a slight modification to closure coefficient values was required. This work demonstrates that it is possible to generate CFD predictions which are highly correlated with the experiential measurements by modifying the turbulence model closure coefficients, and it is possible to tune the standard k-ω SST turbulence model. This work presents the differences between the flow fields around a pre- and post-2017 race-car models using the high fidelity CFD simulations was obtained.

ACKNOWLEDGEMENTS

I would like to thank my thesis advisor Dr. Mesbah Uddin, Director of the NC Motorsports and Automotive Research Center at the University of North Carolina Charlotte. He was always ready to help whenever I had questions about my research or writing. I felt his support and respect for my ideas and desire to point me to the right direction when it was needed.

I would also like to thank the members of my thesis committee, Dr. Peter Tkacik and Dr. Jerre M. Hill, for their involvement and essential input in the evaluation of my research.

My gratitude goes to Joe Gibbs Racing and Toyota Racing Development for providing research facility, data and costly resources that were necessary for the completion of this work.

At last, I would like to express my gratitude to my family for supporting me along the way, encouraging throughout the years of my study, providing help and valuable feedback, which was very important to me. This work would not have been made without them.

TABLE OF CONTENTS

LIST OF TABLES

LIST OF FIGURES

LIST OF ABBREVIATIONS

CAD	Computer-Aided Design
CFD	Computational Fluid Dynamics
JGR	Joe Gibbs Racing
NASCAR	National Association for Stock Car Auto Racing
OpenFOAM	Open source Field Operation And Manipulation
RANS	Reynolds-Averaged Navier-Stokes
TRD	Toyota Racing Development
SST	Shear Stress Transport

CHAPTER 1: INTRODUCTION

Stock car racing organized by National Association for Stock Car Auto Racing (NASCAR) has three major national level series. The most prestigious is Monster Energy NASCAR Cup Series. The Xfinity Series is considered as the final step before entering the top level, and the Gander Outdoors Truck Series is the first step for young drivers in national series.

There are only a few articles published about stock car aerodynamic performance and methods of simulation. Most recent articles were published by Chen Fu et al. (2017, 2018, 2019) where they investigate various turbulence models and effect of closure coefficients on gen 6 NASCAR Cup cars.

Passive and active blowing effects were investigated and published by senior director of aerodynamics at NASCAR Eric Jacuzzi et al. (2018, 2019). Experiments were performed on NASCAR Xfinity cars in order to achieve a more competitive field and interesting racing.

Catranis (2018), in his work, describes cost effectiveness of cloud based CFD simulations on example of 2016 and 2017 NASCAR Xfinity Chevrolet Camaro race cars. This work is the closest to the research and provides additional information for comparison.

FIGURE 1 shows 2016 Toyota Camry NASCAR Xfinity race car on the race track. According to 2016 rules, all cars should have standard spoiler with optional ears attached at the ends. Additionally, all cars should have flat splitter attached at the bottom of front fascia.

Before the beginning of 2017 season NASCAR introduced major aerodynamic rule change for Monster Energy NASCAR Cup Series and Xfinity Series with the intention to reduce aerodynamic forces and improve racing. Due to this change, drivers could not rely as much on vehicles' performance thus putting more importance on driving skills. Spoiler height was reduced, which was supposed to reduce read down force and drag of the vehicle.

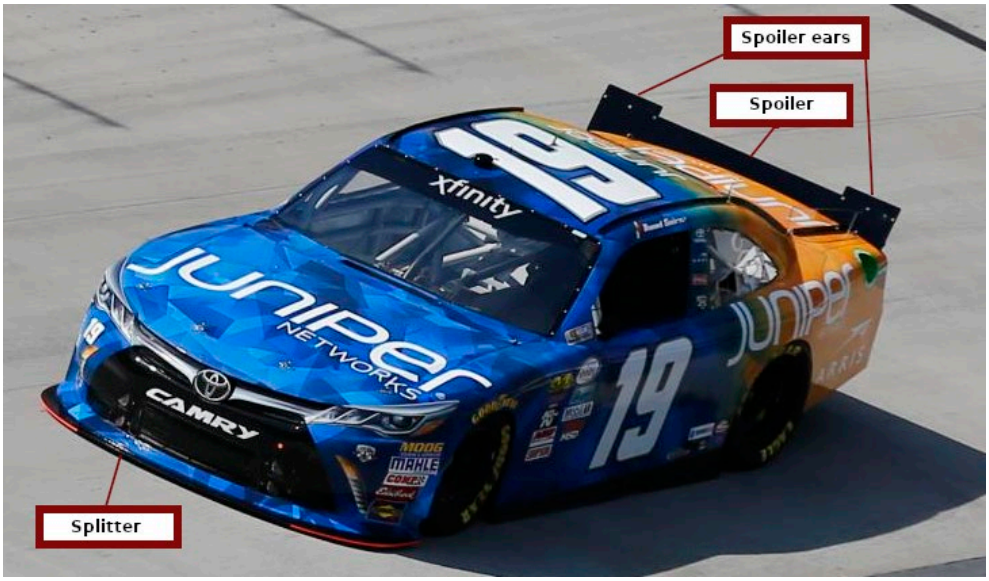

FIGURE 1: 2016 TOYOTA Camry NASCAR Xfinity race car.

FIGURE 2: 2017 TOYOTA Camry NASCAR Xfinity race car.

FIGURE 2 shows 2017 TOYOTA Camry NASCAR Xfinity race car on the race track. Comparing to 2016 aerodynamic rules, 2017 features shorter spoiler with different shape. Spoiler width was also reduced to protect spoiler in the event of hitting a wall on the race track. No spoiler ears became available for 2017 race season. Splitter surface area was also reduced as can be seen on FIGURE 4. An overlay of 2016 and 2017 spoilers is shown on FIGURE 3 to see how both spoilers compare to each other.

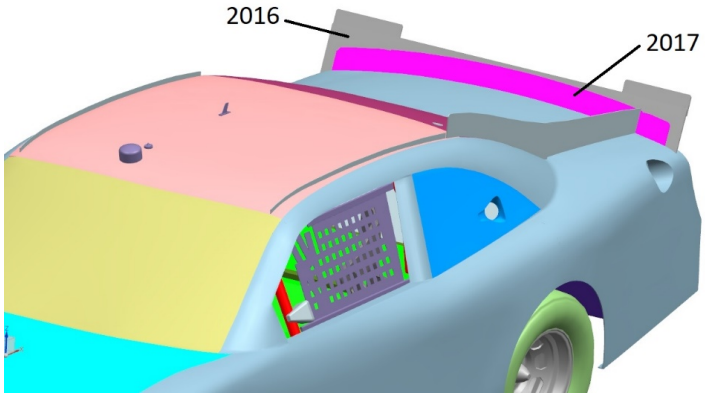

FIGURE 3: 2016 and 2017 Rear spoiler difference.

In order to maintain aerodynamic balance of the car, front down force was reduced by making front splitter 6 in shorter on sides and 2 in shorter in the center, which is shown on FIGURE 4. In order to mimic Monster Energy NASCAR Cup Series rules, splitter height was changed from 5 to 4 inches, which allowed easier inspection process and is shown on FIGURE 5.

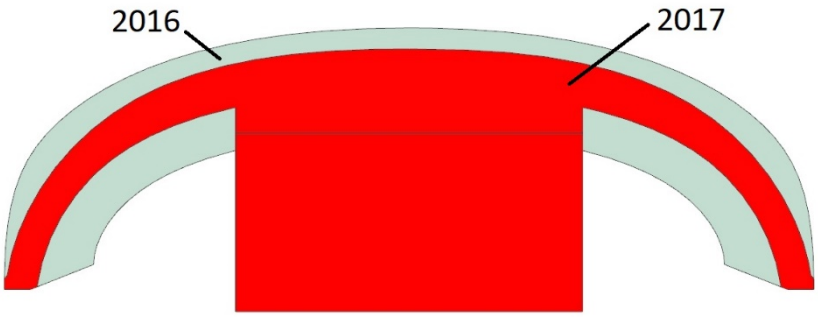

FIGURE 4: 2016 and 2017 Front splitter difference.

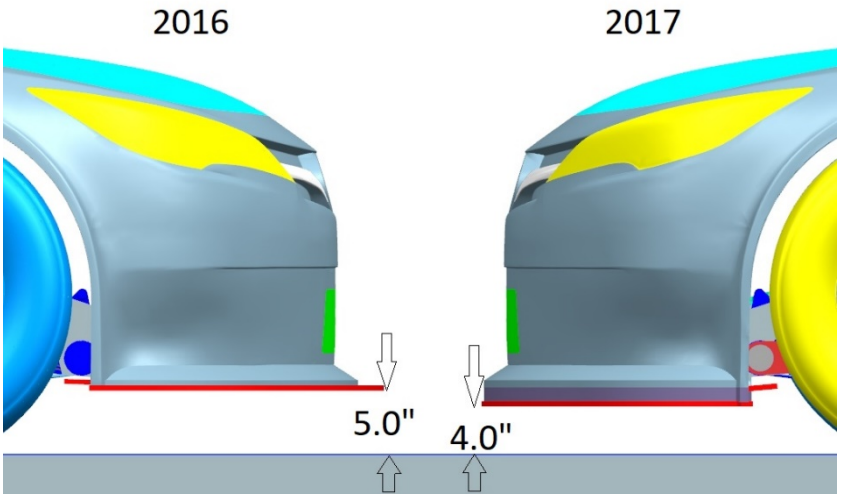

FIGURE 5: 2016 and 2017 Front splitter height difference.

These aerodynamic changes were applied to use at all race tracks, except Daytona International Speedway, Talladega Superspeedway, and Indianapolis Motor Speedway.

1.1 Objective

The main goal of this work is to analyze 2017 NASCAR Xfinity aerodynamic rule changes using RANS approach in CFD simulation. For the simulation it was decided to use only open source software to investigate its capabilities and in case of successful results decrease expenses to perform simulations. To ensure accurate results an exact CAD model of both 2016 and 2017 race cars were created along with full kinematic ride height model. It is well known fact that k-ω SST model tends to predict early separation and as a result larger wake region, but it is able to predict flow structures around race car better than other turbulence models. That is why wind tunnel results were used to improve k-ω SST model. After robust simulation was developed, cars were tested at different ride heights to make sure CFD captures changes in force coefficients and correlated with wind tunnel results. In order to compare aerodynamic performance of

2016 and 2017 cars, a source of largest contributors had to be identified. Detail graphics were used to show changes in pressures and velocity flow fields.

CHAPTER 2: METHODS

An in-depth Computation Fluid Dynamics analysis was performed in order to investigate how the above aerodynamic changes affect vehicle forces in details. This method shows how air flow changes around the car and how it effects local and global forces on the car.

2016 and 2017 aerodynamic devices were compared at different vehicle attitudes. In order to do this in CFD, a comprehensive ride height model that takes into account kinematics of vehicle suspension should be developed. When car goes from one ride height to another, every vehicle component changes its location relative to the wind tunnel. This means that CAD model for every vehicle part needs to be regenerated and exported for CFD simulation. This becomes a huge task considering that there are more than a hundred parts in an assembly. In order to improve this process, it was decided to fix all sprung vehicle components and move wind tunnel and all unsprung components with it. This reduces number of parts that need to be exported only to suspension component and wind tunnel boundaries. Rather than moving car relative to the wind tunnel it was decided to move wind tunnel relative to the car.

Siemens NX CAD software was used to develop all 3d models and export them for CFD simulation. OpenFOAM software package was used to perform CFD simulation. This package consists of snappyHex mesher, OpenFOAM solvers, and ParaView post processing tools. Mesher allows to split volume around the car in a virtual wind tunnel into hexahedral cells. Solver uses this mesh to perform calculation and pass flow properties between cells. Post processing tool helps to visualize data and generate plots and figures. Surface flow was compared to flow visualization data from wind tunnel.

Global drag, down-force, and side-force were also compared to coefficients obtained during wind tunnel tests for both 2016 and 2017 aerodynamic packages.

Using only open source software introduces additional challenges. Not many open source meshers are able to produce hexahedral or polyhedral mesh in excess of 120M cells. Mesher should be able to support parallel processing. Additionally, mesher should be able to produce boundary layers with specified thickness. Based on these requirements snappyhexMesh was chosen. It does not have graphical interface and all settings should be provided in dictionary file. This allows users to modify dictionary files and create user defined scripts in order to generate custom meshes.

OpenFOAM grew in popularity over the past decade as an open source CFD software that is comparable to commercial analogs. It has wide variety of solvers for different types of simulation.

ParaView data visualizing software was used for post-processing. It is also available to the public without any cost. Same as snappyHexMesh and OpenFOAM, it is customizable and allows for custom script development in order to make post-processing automatic.

Radiator properties were modeled as porous media using Darcy law. Pressure drop coefficients were measured during wind tunnel experiment and used to calculate Darcy law coefficients.

During 2017 rule change splitter was 1 inch lower which resulted in higher vehicle body position compared to 2016 rule package at the same splitter heights. Since splitter height is more dominant in aerodynamic performance, it was chosen to compare

different aerodynamic packages at common splitter gaps rather than common body position.

2.1 Theory

To perform steady state, incompressible, and isothermal CFD simulation, OpenFoam utilizes continuity equation (1) in combination with Navier-Stokes momentum equation.

$$\frac{\partial u}{\partial x} + \frac{\partial v}{\partial y} + \frac{\partial \omega}{\partial z} = 0 \tag{1}$$

$$\rho[\frac{\partial u_i}{\partial t} + \frac{\partial}{\partial x_j}(u_i u_j)] = \frac{\partial p}{\partial x_i} + \frac{\partial}{\partial x_j}(\mu \frac{u_i}{\partial x_j}) \tag{2}$$

In order to solve these equations a Reynolds average decomposition is applied where each unknown component is decomposed into average and fluctuating components.

$$p = \bar{p} + p' \tag{3}$$
$$u = \bar{u} + u' \tag{4}$$
$$v = \bar{v} + v' \tag{5}$$
$$w = \bar{w} + w' \tag{6}$$

Remolds Average Navier-Stokes equations obtains the following form:

$$\rho[\frac{\partial \bar{u}_i}{\partial t} + \frac{\partial}{\partial x_j}(u_i u_j)] = \frac{\partial \bar{p}}{\partial x_i} + \frac{\partial}{\partial x_j}(\mu \frac{\partial \bar{u}_i}{\partial x_j} - \rho\overline{u_i' u_j'}) \tag{7}$$

An extra term in the end ($\rho\overline{u_i' u_j'}$) is called Reynolds stress. It is composed of normal and shear stresses. Turbulence modeling is aimed to represent these stresses in terms of average velocity components.

SST k-ω model introduces two additional equations to solve close this problem. Turbulent kinetic energy equation (8) and turbulence dissipation equation (9).

$$U_j \frac{\partial k}{\partial x_j} = P_k - \beta^* k\,\omega + \frac{\partial}{\partial x_j}[(\nu + \sigma_k \nu_t) \frac{\partial k}{\partial x_j}] \tag{8}$$

$$U_j \frac{\partial \omega}{\partial x_j} = aS^2 - \beta \omega^2 + \frac{\partial}{\partial x_j}[(\nu + \sigma_\omega \nu_{t)} \frac{\partial \omega}{\partial x_j}] + 2(1 - F_1)\sigma_{\omega 2} \frac{1}{\omega} \frac{\partial k}{\partial x_i} \frac{\partial \omega}{\partial x_i} \quad (9)$$

Where:

$$P_k = \min(\tau_{ij} \frac{\partial U_i}{\partial x_j}, 10\, \beta^* k\omega) \quad (10)$$

$$\nu_t = \frac{a_1 k}{\max(a_1 \omega, SF_{2)}} \quad (11)$$

$$F_1 = \tanh\{\{\min[\max(\frac{\sqrt{k}}{\beta^* \omega y}, \frac{500\nu}{y^2 \omega}), \frac{4\rho)\sigma_{\omega^2} k}{CD_{k\omega} y^2}]\}^{4}\} \quad (12)$$

$$CD_{k\omega} = \max(2\rho\sigma_{\omega 2} \frac{1}{\omega} \frac{\partial k}{\partial x_i} \frac{\partial \omega}{\partial x_i}, 10^{-10}) \quad (13)$$

$$F_2 = \tanh[[\max(\frac{2\sqrt{k}}{\beta^* \omega y}, \frac{500\nu}{y^2 \omega})]^{2}] \quad (14)$$

$$\tau_{ij} = \mu_t (2S_{ij} - \frac{2}{3} \frac{\partial u_k}{\partial x_k} \delta_{ij} - \frac{2}{3} \rho k \delta_{ij} \quad (15)$$

$$\bar{S}_{ij} = \frac{1}{2} (\frac{\partial \bar{U}_i}{\partial x_j} + \frac{\partial \bar{U}_j}{\partial x_i}) \quad (16)$$

$$S = \sqrt{2 S_{ij} S_{ij}} \quad (17)$$

σ_{k1} =0.85 σ_{k2} =1.0 $\sigma_{\omega 1}$ =0.5 $\sigma_{\omega 2}$ =0.856 β*=0.09

k=0.41 a_1 =0.31 β_1 = 0.075 β_2 = 0.0828

CHAPTER 3: GEOMETRY

Toyota Camry NASCAR Xfinity Series race car was chosen for the simulation. This model was introduced in 2015 and was used until the end of 2018 when it was replaced with Toyota Supra NASCAR Xfinity Series race car. FIGURE 6 shows 2015 Toyota Camry.

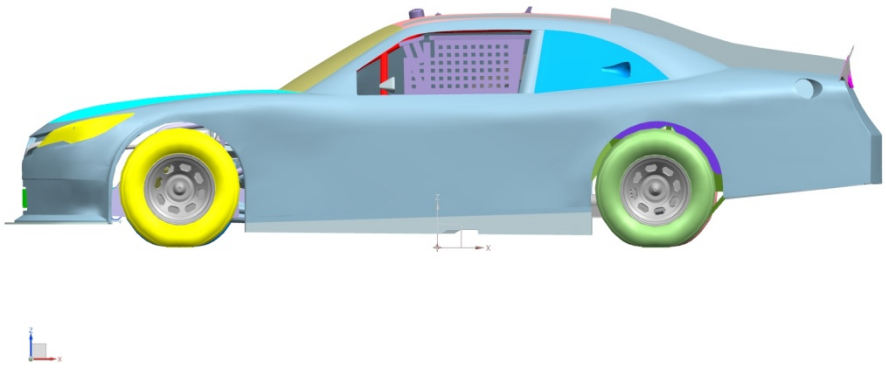

FIGURE 6: NASCAR Xfinity racing series Toyota Camry.

In order to obtain accurate 3D model of a car, it was scanned using white light scanner that produces point cloud within 0.002” from actual surface. This point cloud was cleaned from unwanted data. Then, it was surfaced and thickened, which produced clean, closed volume that is perfectly suited for CFD simulations. Following of this process ensures fully accurate vehicle representation. After this, it is critically important to position vehicle in the wind tunnel at exactly same attitude. To achieve this, a kinematic ride height model was developed. This model takes splitter to ground distance as an input to set front ride height and rear wheel travel from inspection ride height to set rear ride height. Additionally, yaw angle of a wind tunnel is set at this stage. The

boundaries of wind tunnel were set 20 meters in-front of the car, 50 meters behind, 20 meters above, to the left, and to the right from the car. Computational domain is shown on FIGURE 7.

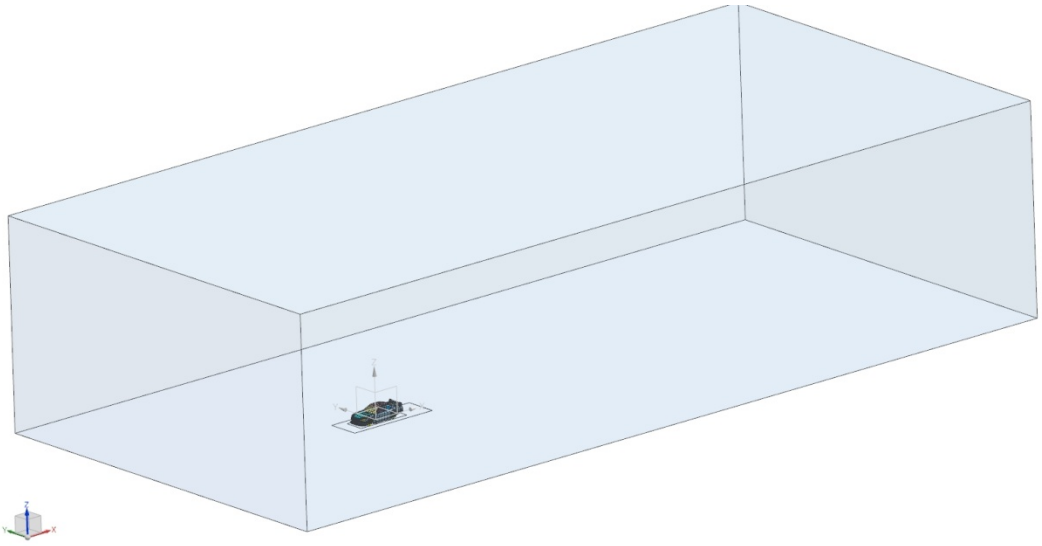

FIGURE 7: Computational domain.

3.1. Mesh

Mesh was generated using SnappyHexMesh utility in OpenFOAM. This utility takes *.stl files as an input. This means that all vehicle parts along with wind tunnel boundaries should be exported in separate files. Later each file is assigned its own boundary conditions.

First step in mesh generation is creation of background mesh. It is important that all vehicle parts and wind tunnel walls are fully included in background mesh. In order to do so, far most corners of the rectangular domain should be specified along with number of cells in each direction. It is critical for successful mesh to make sure that all sides of a single cell are even. Background mesh is also called level zero as it is the coarsest mesh

in the entire domain. For this simulation base mesh size was selected to be 0.25m. Mesh is refined in levels when each 3d cell is divided into 8 cells. Level one cells are 0.125m, level two cells are 0.0625m and so on.

Mesh can be refined using volume source. During this process a volume can be resized to a desired level inside a specific geometry. Volume refinement regions are shown on FIGURE 8. Another way to refine volume is by specifying distance form an object. Every cell that lies within specified distance is refined to assigned level. The combination of volume refinement and distance from surface refinement features were used for all simulations.

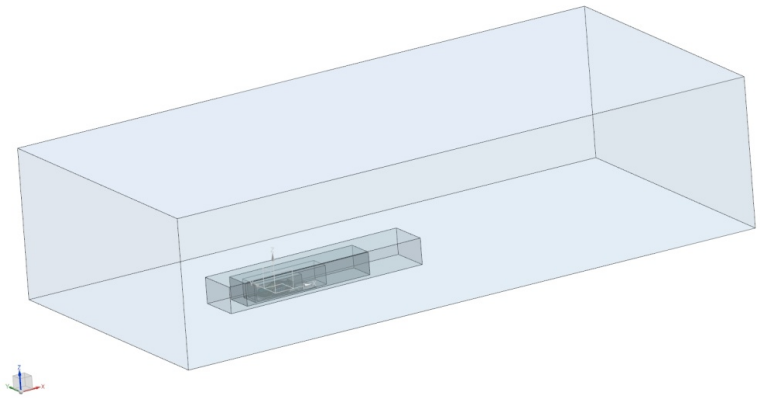

FIGURE 8: Volume refinement regions.

Surface refinement is also done in a similar way. To do so maximum and minimum cell levels need to be specified for surface refinement. Based on the curvature parameter, algorithm decides whether cell size could be closer to minimum or maximum levels. If curvature of the surface is high, then surface is refined to maximum specified level, and if curvature is low, cells are refined to minimum level. FIGURE 9 shows

surface mesh refinement around left headlight. Surface maximum refinement level is 6 (4mm) and minimum refinement level is 7 (2mm).

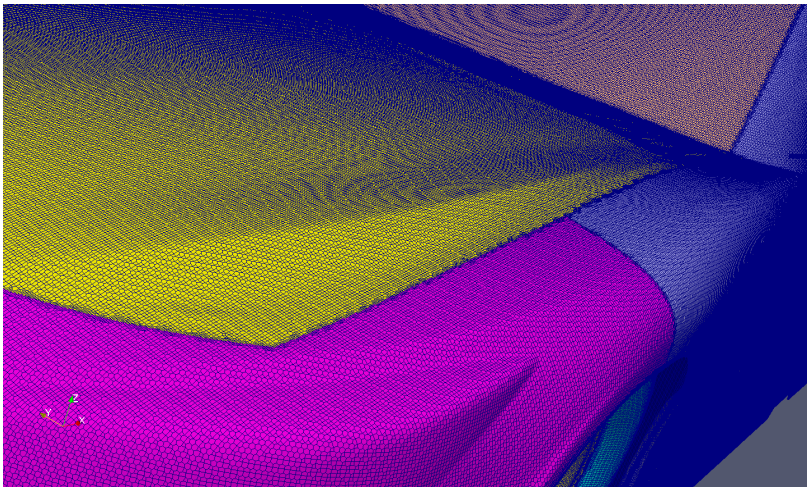

FIGURE 9: Surface mesh.

There are several critical areas for volume refinement. These areas can be separated into 3 categories. First category includes areas where high velocity gradient is present. They are mostly concentrated around aerodynamic devices like splitter and spoiler and around wheel contact patches. Second category includes flow in a wake region. Wake is mostly concentrated behind the car. Third category consists of areas around sharp edges or thin sheet metal parts. Fender wheel openings, skirts, antennas, brake rotors, roof rails, and fins fall into this category.

In order to capture all details of the car, surface refinement with additional edge refinement are used. Edge refinement ensures that all edges are sharp and well defined. Similar to volume refinement, surface should be refined on aerodynamic devices and on thin surfaces. Car body surface was refined to 4mm while splitter and spoiler were refined to 2mm with edge refinement down to 1mm. Most thin surfaces and sharp edges were refined to 1mm. Volume mesh plot with distance from surface refinement is shown

on FIGURE 10. This technique allows gradual transition from background mesh of level 0 to surface mesh levels. FIGURE 11 shows volume mesh with volume refinement. This technique is used to refine wake region behind the car.

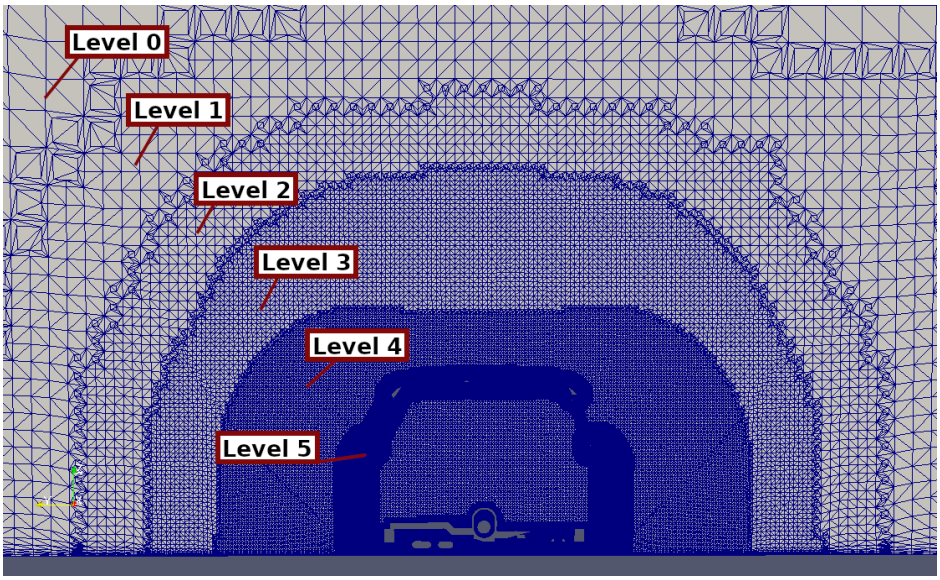

FIGURE 10: Volume mesh plot slice through y-z plane.

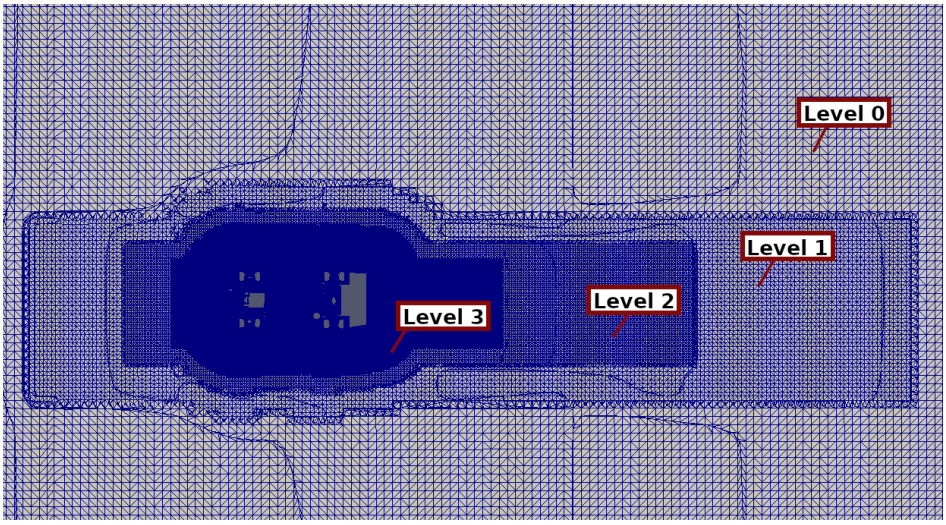

FIGURE 11: Volume mesh plot slice through x-y plane.

FIGURE 12 shows zoomed-in view of volume mesh around the car on x-z plane. This view allows to see how refinement levels change as distance from car surface approaches zero. Additionally, volume under the car is refined to level 5 and 6 as high velocity gradient is present there which is related to under-body center jet flow and its dissipation. Capturing jet dissipation is critical for force coefficients prediction which will be shown in results section.

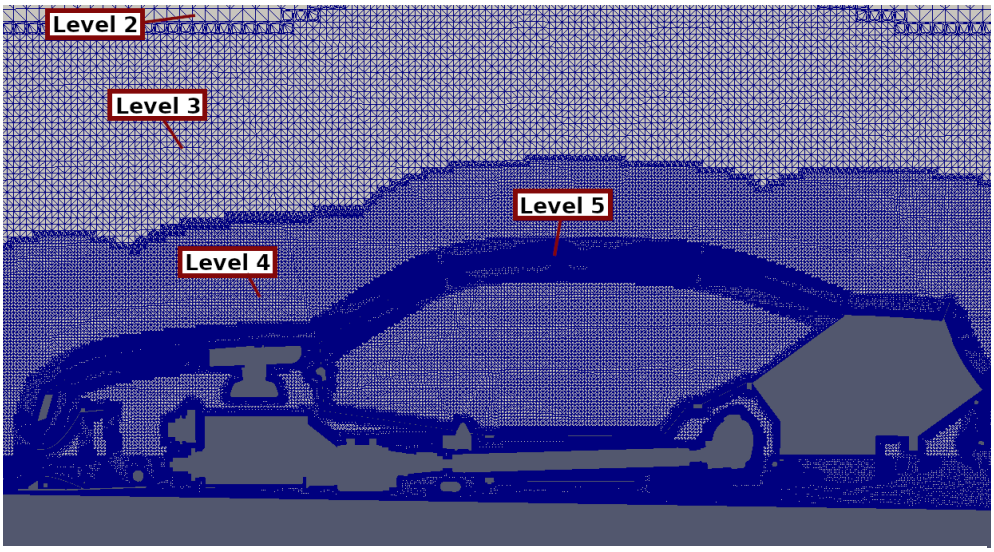

FIGURE 12: Volume mesh plot slice through x-z plane.

The most important area for refinement is around front splitter as the highest pressure and velocity gradients are observed there. That is why splitter surface was refined to level 7 and 8 which is 1-2 mm cell size. Volume was refined to level 7 (2mm cell size). The following figure shows volume refinement around splitter leading edge. The gap between splitter and ground has at least 10 cells vertically.

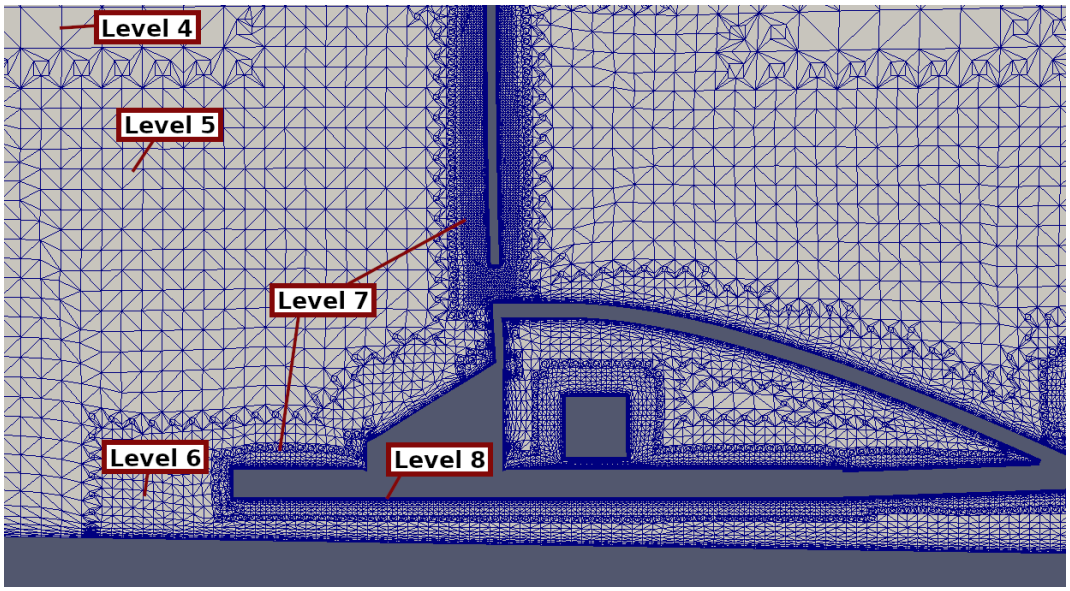

FIGURE 13: Splitter volume mesh plot slice through x-z plane.

3.2. Boundary Conditions

Average speed of the NASCAR Xfinity Series race car around 1.5 miles track is 180 mph. That is why it was decided to perform simulation at this speed. Ground velocity was also set at the same magnitude and directions as the air flow. Tire surfaces were assigned tangential velocity to match that of the ground. Similarly, all rotational components had the same angular velocity as tires. For the inlet it was chosen to use turbulence intensity of 0.2% and turbulent viscosity ratio of 10.

3.3. Simulation

Taking significant mesh size and limited computing resources into consideration, it is not practical to perform any other type of simulation than RANS. It provides steady state flow field results for incompressible fluid in this case because maximum velocity is less than 0.3M. Air density is considered constant through the domain with viscosity selected at 20 degrees C at 1.5e-5 m^2/s. Turbulence model was selected to be k-ω -SST based on previous research by Chen Fu et al. (2019). According to his work it is the only

turbulence model that was able to capture changes in force coefficients due to change in vehicle ride height and yaw angle. Jacuzzi and Catranis also used the same turbulence model for their simulations. This model has an ability to over-predict the size of wake region and tends to predict early separation. This issue will be addressed by modifying turbulence coefficient to match wind tunnel results.

3.4. Settings

Selecting numerical discretization scheme is critical. The most popular and robust schemes that gained popularity for external flow are first and second order upwind schemes. These two schemes were compared to wind tunnel experiment. The emphasis is put on global force coefficients and flow pattern near the surface. Both schemes were very close to each other on predicting force coefficients. The biggest difference was observed in surface flow pattern in separation regions. Second order scheme produces flow pattern, which is very similar to wind tunnel experiment. The biggest discrepancy was observed in the prediction of separation bubble. Second order separation was too large comparing to experiments. First order scheme failed to predict separation at all. That is why second order was chosen for further simulations. I will attempt to correct early separation with turbulence model and its coefficients.

Porous media was used to simulate radiator flow using Darcy's law. Pressure drop and velocity ratios were measured in front and behind radiator during wind tunnel experiment. Using this data, coefficients were calculated for d and f vectors. Vectors e1 and e2 are assigned based on radiator orientation.

CHAPTER 4: RESULTS AND DISCUSSION

First simulation was performed at ride height 1 (RH1) using standard turbulence model closure coefficients. Wall shear stress along with near the surface stream lines are shown on FIGURE 14. There is significant separation of the flow at the rear glass. The size of the separation bubble on the right side was measured during wind tunnel experiment and has a longitudinal dimension of **d.** According to standard turbulence model the separation bubble length is over-predicted by 30%.

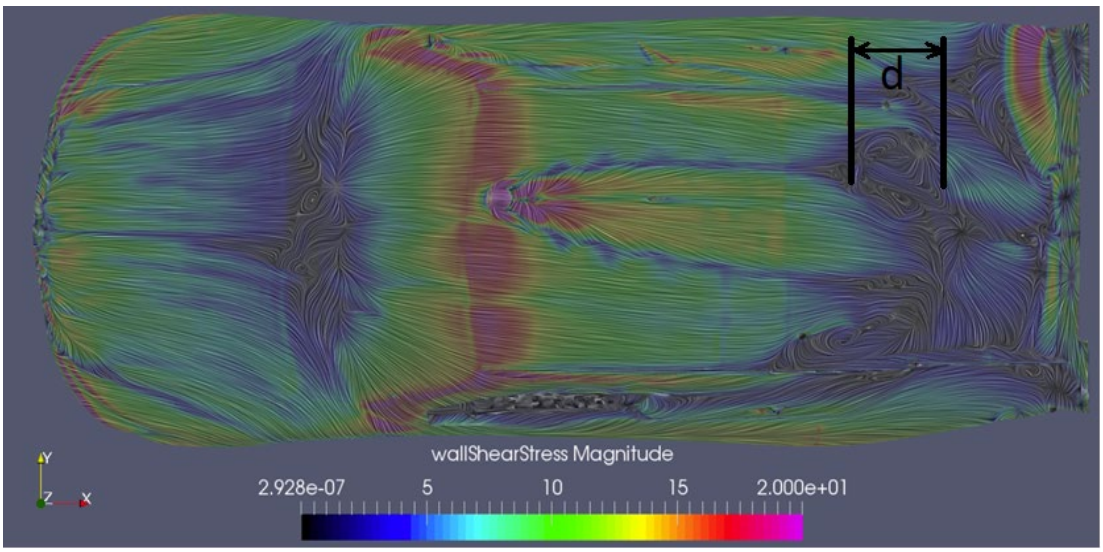

FIGURE 14: Wall shear stress and oil flow lines (a1=0.31).

Early separation leads to under-prediction of force coefficients when compared to wind tunnel results. TABLE 1 shows the difference between wind tunnel results and standard k-ω SST model CFD results.

The biggest difference between wind tunnel and CFD results is in prediction of drag and rear lift coefficient. Separation on the rear glass effects mostly rear down-force and drag. That is why by reducing separation, drag and down-force will improve.

TABLE 1: Standard *k-ω* -SST model CFD results vs wind tunnel results.

	Cd	Cl	Clf	Clr	Cs	%F	L/D
Wind Tunnel	0.474	-0.929	-0.423	-0.506	-0.189	45.5%	-1.960
CFD	0.404	-0.832	-0.389	-0.443	-0.182	46.7%	-2.062
Difference	14.9%	10.4%	8.0%	12.4%	3.7%	-1.2%	-5.2%

In order to decrease separation, turbulence viscosity needs to increase in the wake region. The simplest way to do this is to increase a1 coefficient in turbulent viscosity equation. Standard value of a1 coefficient is 0.31. The best results were obtained when a1 was increased to 0.5. Further increase in a1 coefficient did not provide significant improvement. When a1=0.5, separation on rear glass was reduced to match wind tunnel results exactly.

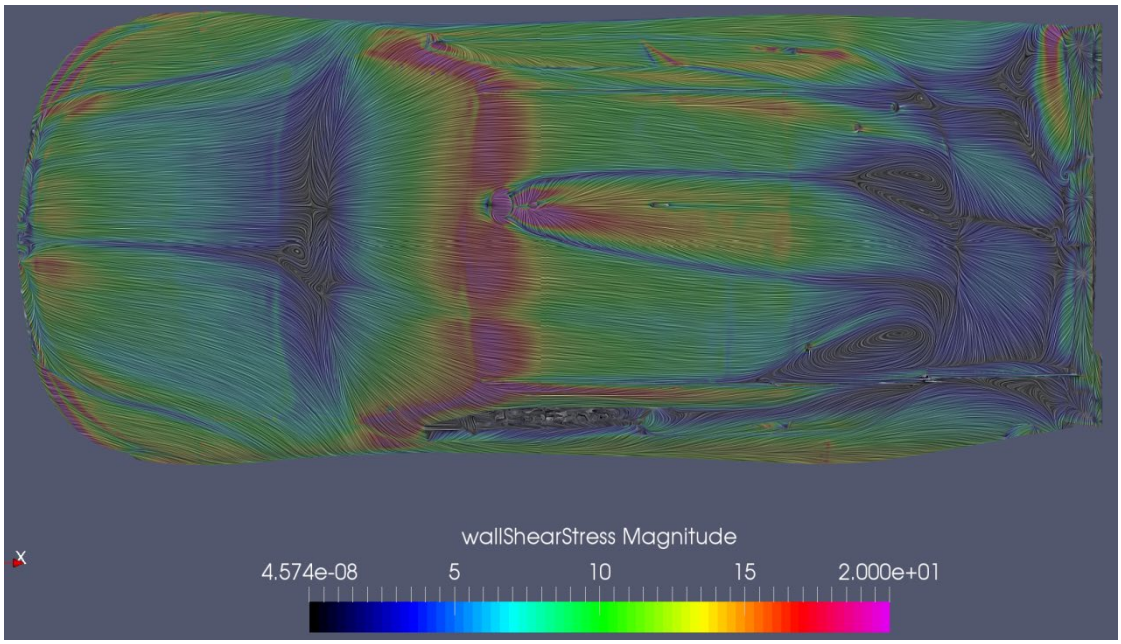

FIGURE 15: Wall shear stress and oil flow lines (a1=0.5).

Force coefficients were also improved by increasing a1 coefficient. TABLE 2 shows how modified model correlates to wind tunnel results. Lift coefficient is within 1% from experimental results. Drag coefficient is 10.8 % lower than experimental results but it is a 4.1% improvement comparing to drag estimated using standard a1 coefficient. Vehicle down-force balance along with side-force coefficient were accurately predicted within 1%.

TABLE 2: Modified k-ω SST model CFD results vs wind tunnel results.

	Cd	Cl	Clf	Clr	Cs	%F	L/D
Wind Tunnel	0.474	-0.929	-0.423	-0.506	-0.189	45.5%	-1.960
CFD	0.423	-0.934	-0.419	-0.515	-0.188	44.8%	-2.209
Difference	10.8%	-0.5%	1.0%	-1.7%	0.5%	0.7%	-12.7%

Mesh size can have its influence on flow results. This influence decreases with an increase in mesh size. In order to make sure that mesh is sufficiently large, numerous simulations were performed using different level zero cell size. Other mesh parameters were kept constant. For level zero cell size of 0.29m overall mesh size was 77M cells. For base mesh size of 0.27m cell count increased to 94M, for base size of 0.25m mesh increased to 122M cells. Refining past 94M cells did not show significant improvement. TABLE 3 shows how force coefficients change with increase in cell counts.

TABLE 3: Mesh sensitivity.

Mesh	Cd	Cl	Clf	Clr	%F	Cs	Cells
Coarse	0.420	-0.919	-0.414	-0.505	45.0%	-0.181	77085720
Medium	0.423	-0.934	-0.419	-0.515	44.8%	-0.185	94733708
Fine	0.421	-0.931	-0.419	-0.512	45.0%	-0.184	122828791

Changing mesh size from 77M to 122M did not have any influence on drag and side-force coefficients. The variation was not more than 4 counts. Lift coefficient was more sensitive to mesh size.

The difference between 77M and 94M meshes, which was about 20%, resulted in 1.6% change in lift coefficient. Further increase in cell counts by 20% to 122M mesh showed 0.35% difference in lift coefficient prediction. 122M cell mesh requires 20% more in computational resources when compared to 94M cell mesh. At the same time results obtained using fine and medium meshes were within 0.35%. That is why 94M cell mesh was considered optimum.

By this point, a simulation that has good correlation with experimental results and independent of mesh size was established. To validate simulation configuration, vehicle ride height was changed to RH2 and the results were compared to the wind tunnel experiment. Changing ride height of the car significantly effects the flow around the car. Maintaining good correlation with experimental results ensures validity of modified turbulence model. TABLE 4 shows force coefficients produced by the car at ride height RH2.

TABLE 4: Force coefficients at ride height RH2.

	Cd	Cl	Clf	Clr	Cs	%F	L/D
Wind Tunnel	0.497	-1.044	-0.514	-0.530	-0.200	49.2%	-2.101
CFD	0.460	-1.069	-0.513	-0.557	-0.186	48.0%	-2.323
Difference	7.4%	-2.4%	0.2%	-5.0%	6.8%	1.2%	-10.5%

Ride height RH2 produces significantly more down-force and drag when compared to RH1. At the same time there is approximately 4% shift in down-force balance to the front. CFD simulation was able to predict these changes in body forces and improve drag correlation.

After establishing simulation that can accurately calculate force coefficients and simulate flow around 2016 TOYOTA Camry, a 2017 aerodynamic package can be simulated with great confidence.

By reducing the size of aerodynamic devises, decrease in body forces on the vehicle should be expected. Simulation was performed at ride height RH2 and compared to wind tunnel results. TABLE 5 provides these results.

TABLE 5: Force coefficients at ride height RH2.

	Cd	Cl	Clf	Clr	Cs	%F	L/D
Wind Tunnel	0.429	-0.794	-0.365	-0.429	-0.183	45.9%	-1.850
CFD	0.384	-0.767	-0.343	-0.424	-0.184	44.7%	-2.000
Difference	10.7%	3.4%	6.0%	1.2%	-0.3%	1.2%	-8.2%

Similar to previous results, drag coefficient is under-predicted by about 10%. On the positive side, down-force and side-force have great correlation with experimental results along with the prediction of front to rear down-force balance. FIGURE 16 shows how force coefficients compare between 2016 and 2017 aerodynamic rule packages.

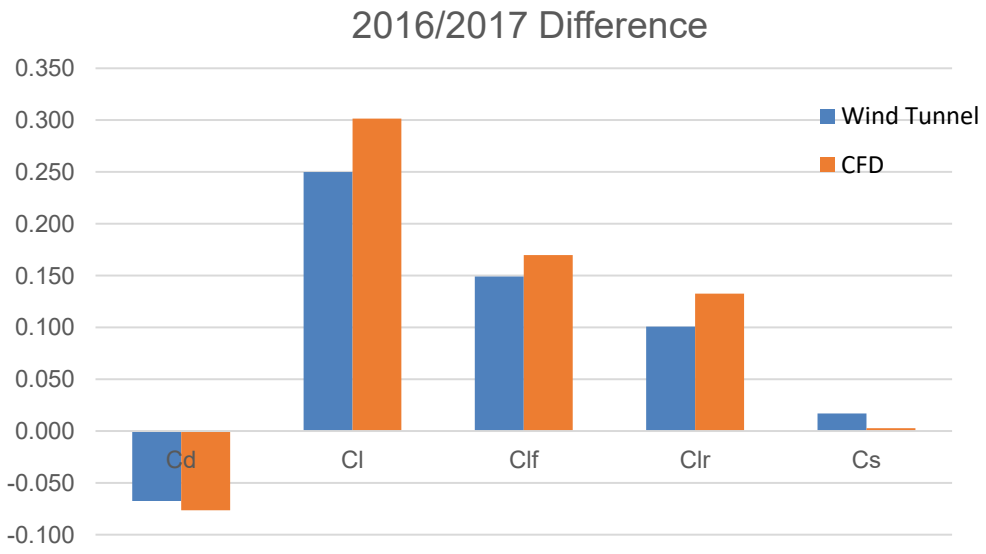

FIGURE 16: Difference between 2016 and 2017 aerodynamic rule packages.

CFD simulation was able to predict the trend that was recorded during wind tunnel test when comparing 2016 and 2017 aerodynamic packages. In order to further

investigate, where the difference between rule packages is coming from, I measured how much each vehicle component is contributing to a total of drag and lift coefficient for 2016 and 2017 cars. The difference in drag contribution is shown of FIGURE 13, and lift coefficient difference is shown on FIGURE 17.

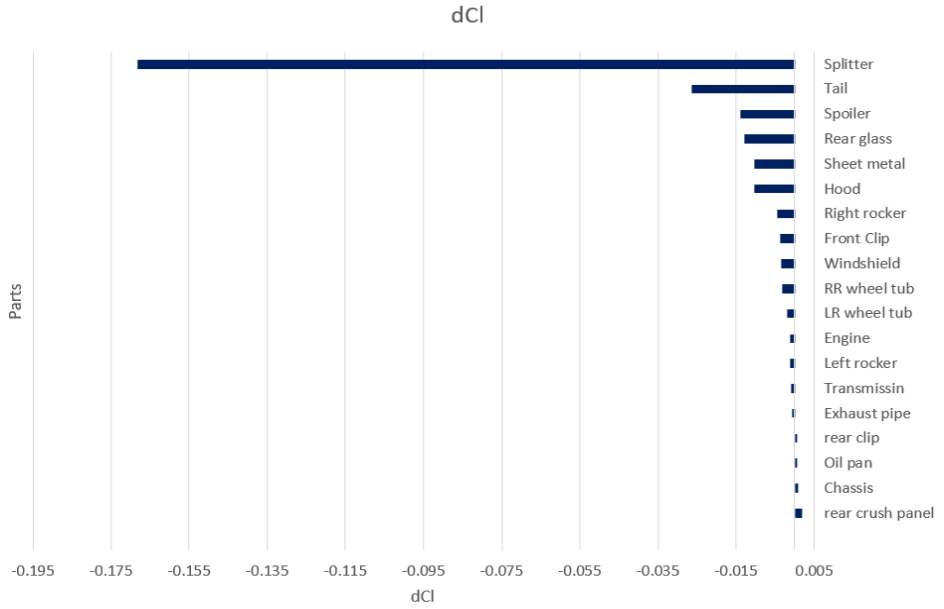

FIGURE 17: Drag coefficient difference contribution by parts.

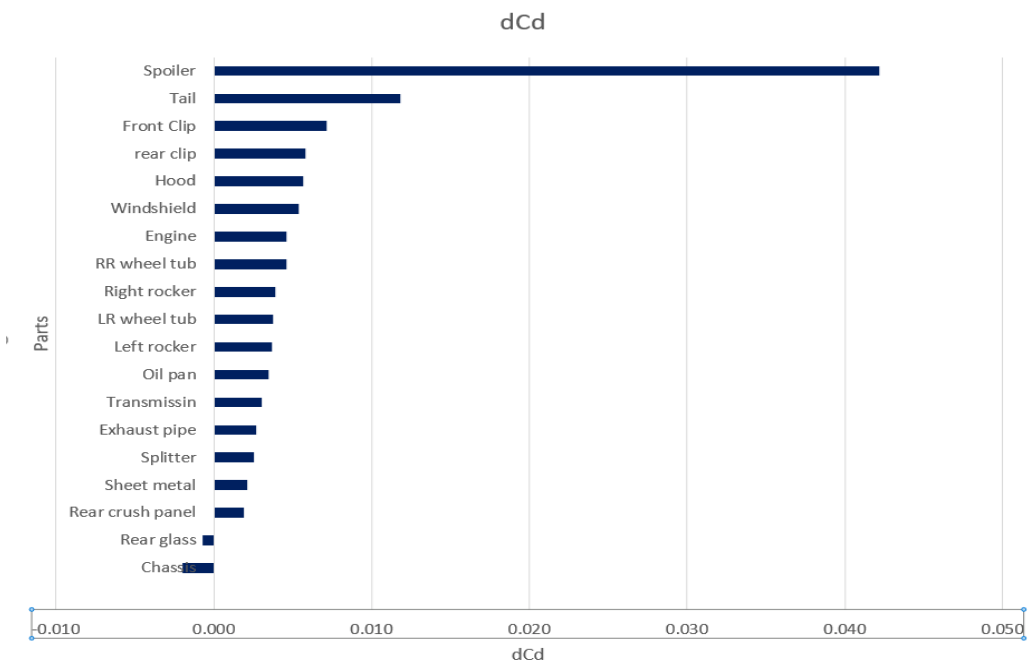

FIGURE 18: Lift coefficient difference contribution by parts.

From FIGURE 18 it becomes clear that most of the drag penalty is coming from rear spoiler. It is solemnly responsible for 42 counts of drag penalty on 2016 car. Rear spoiler itself only produces 14 counts of down-force, but it is also responsible for pressure build up on top of the tail, which results in additional 26 counts of down-force. It is not the rear spoiler that is responsible for majority of down-force difference. Front splitter on 2016 car generates 168 counts of down-force more than 2017 splitter, while producing only 3 more counts of drag.

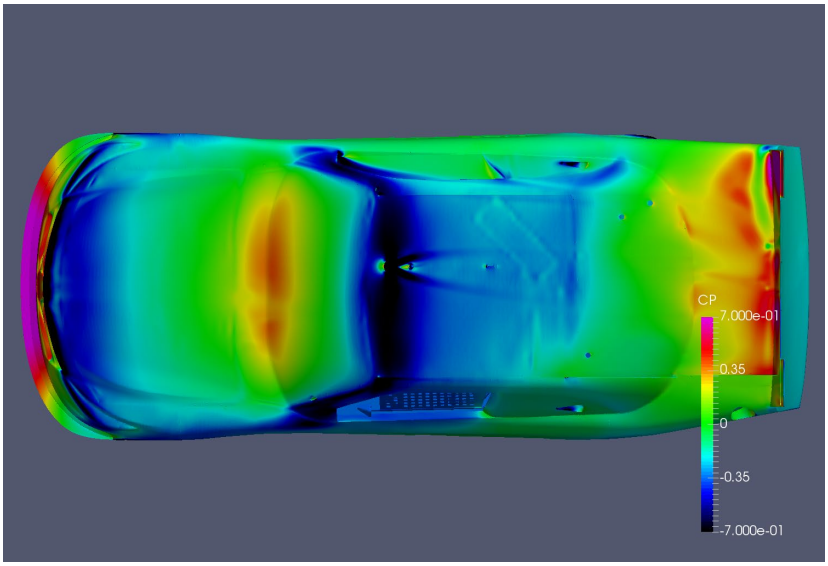

FIGURE 19: Pressure coefficient distribution over 2016 Toyota Camry.

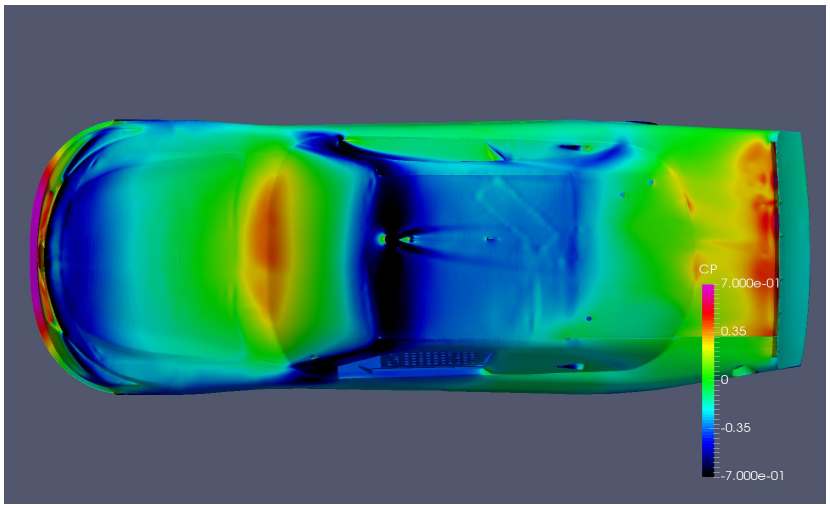

FIGURE 20: Pressure coefficient distribution over 2017 Toyota Camry.

FIGURES. 19 and 20 show pressure distribution over the top of 2016 and 2017 cars. Pressures are very similar between the two cars. The only difference is observed near rear spoiler. Additionally, 10 pressure sensors were placed underneath the car and six sensors were placed on top of the deck lid to measure pressure difference between both cars. Pressure sensor array is shown on Figs. 21 and 22. The data from these sensors is represented on FIGURE 23.

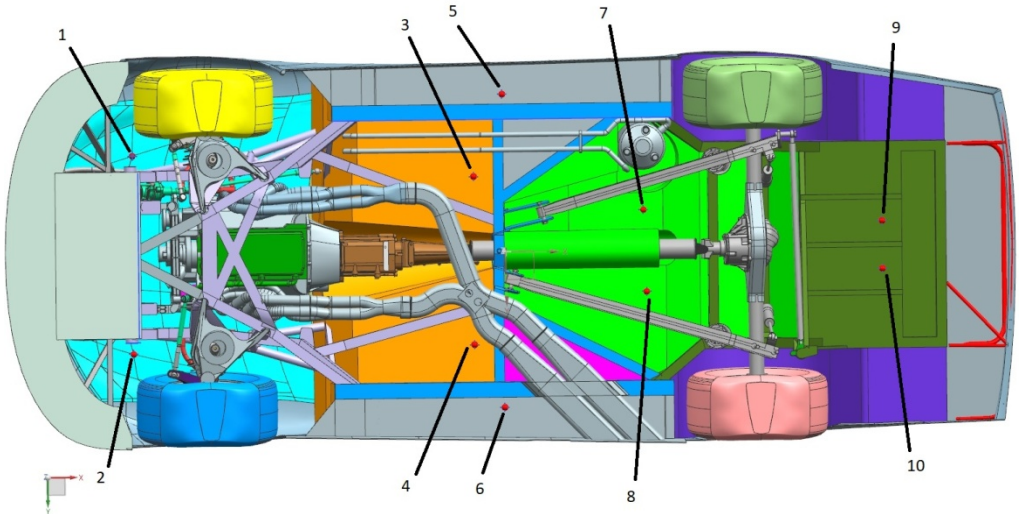

FIGURE 21: Pressure sensor array underneath the car.

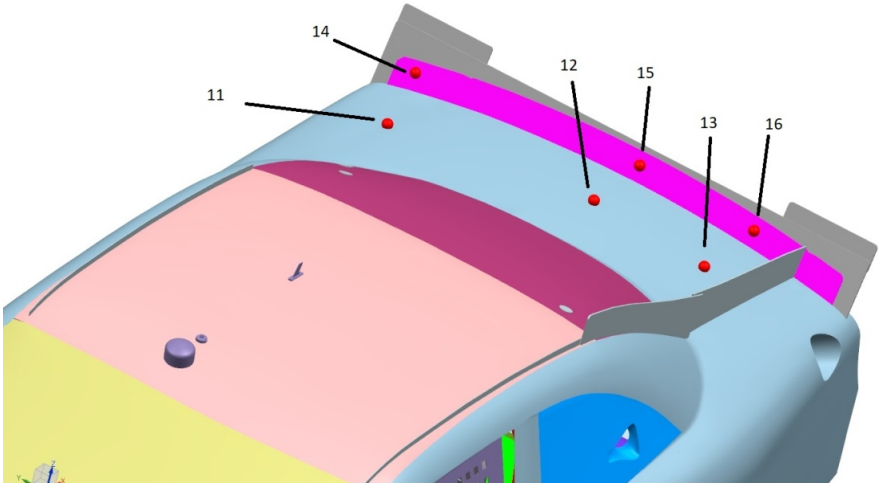

FIGURE 22: Pressure sensor array on top of the deck lid.

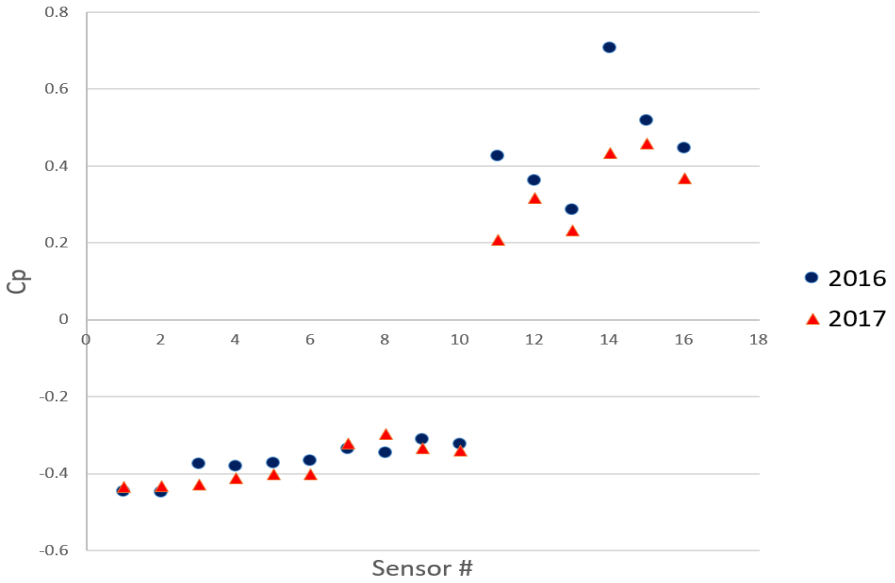

FIGURE 23: Pressure sensor data.

Based on the data from sensors 1 and 2, 2016 rule package results in lower pressure under the hood. Considering large area of the hood, small pressure decrease under the hood resulted in 10 counts of down-force increase in 2016 car favor. Similarly, under the rocker panels and front floor boards the 2016 car had higher pressure, which decreased under rear floor boards then went up under the fuel cell. Overall, floor boards did not show significant pressure change between 2016 and 2017 cars but because of the significant area that the floor board occupies, on average, small pressure decrease resulted in 10 more counts of down-force on the 2016 car. Pressure distribution underneath the 2016 car is shown on FIGURE 24 and underneath the 2017 car on FIGURE 25. On contrast, by measuring pressures on the top of the deck lid, a significant drop in pressure was noticed on the 2017 car. Taller spoiler on 2016 car captures more air on top of rear deck lid, which increases pressure on it and produces increase in rear down-force.

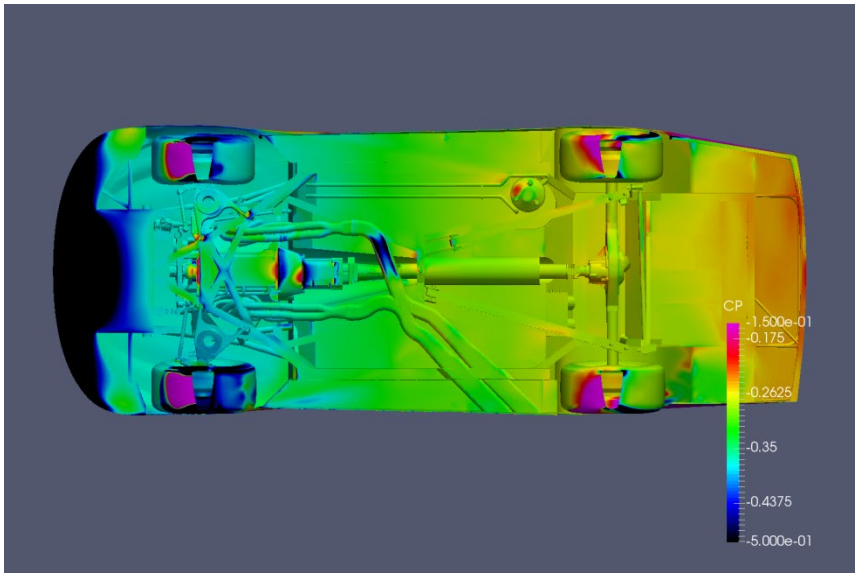

FIGURE 24: Pressure coefficient distribution under 2016 Toyota Camry.

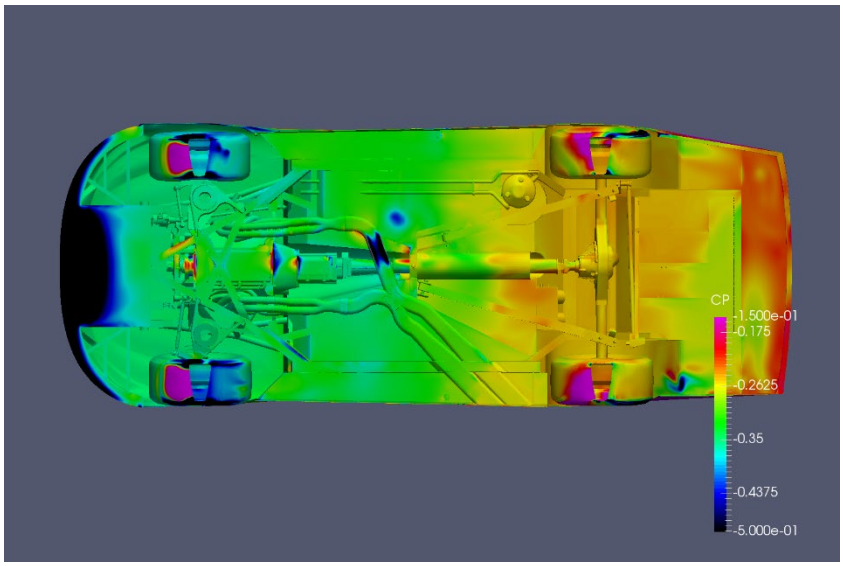

FIGURE 25: Pressure coefficient distribution under 2017 Toyota Camry.

Longer splitter overhang on the front of 2016 car captures high pressure air on top of the splitter that increases front down-force. Pressure on top of the splitter does not change significantly between the aero packages, and minimum pressure under two different splitters is about the same. 2016 splitter has large area that captures high

pressure on top and low pressure on the bottom which results in down-force difference. FIGURE 26 shows splitter centerline pressure for 2016 and 2017 configurations.

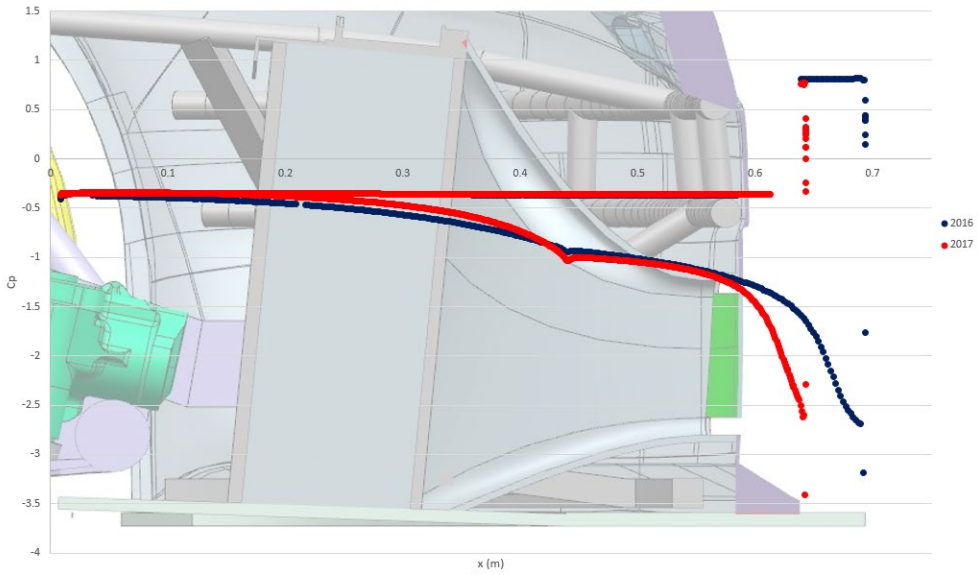

FIGURE 26: Splitter centerline pressure.

Zero point on x-axis was chosen to be at the trailing edge of the splitter since both 2016 and 2017 splitters begin at the same location. Minimum pressure on the bottom of both splitters is very similar. Maximum pressure on the top of both splitters is also the same. The only difference is that 2016 splitter leading edge is far more forward, which allows it to capture greater area of high pressure on top of the splitter and low pressure on the bottom.

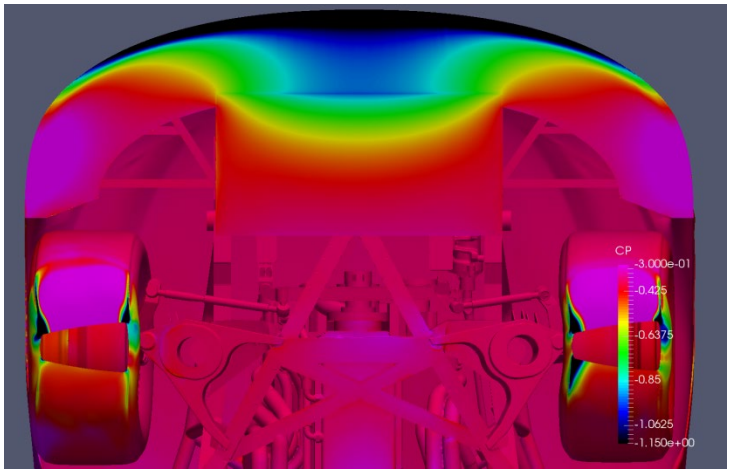

FIGURE 27: Pressure coefficient distribution under 2016 splitter.

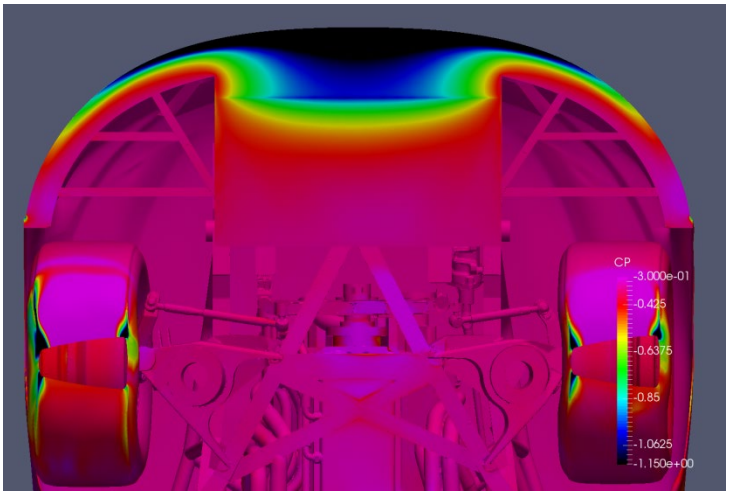

FIGURE 28: Pressure coefficient distribution under 2017 splitter.

Similar trend is observed along the entire leading edge of the splitter and is represented in Figs. 27 and 28. Having a splitter extend extra 2 inches forward on 2016 car resulted in significant 168 counts increase in down-force. Additionally, longer splitter side wings help to keep air from filling the under hood area, thus reducing pressure there and increasing down-force. This air is used to energize under-body jet flow. In order to compare under-body flow for the 2016 and 2017 cars, a cut plane plots were created where the plane is passing through the center of splitter gap (h) parallel to the ground.

FIGURE 29 shows velocity magnitude plot for the 2016 car under-body center jet and FIGURE 30 - for the 2017 under-body center jet.

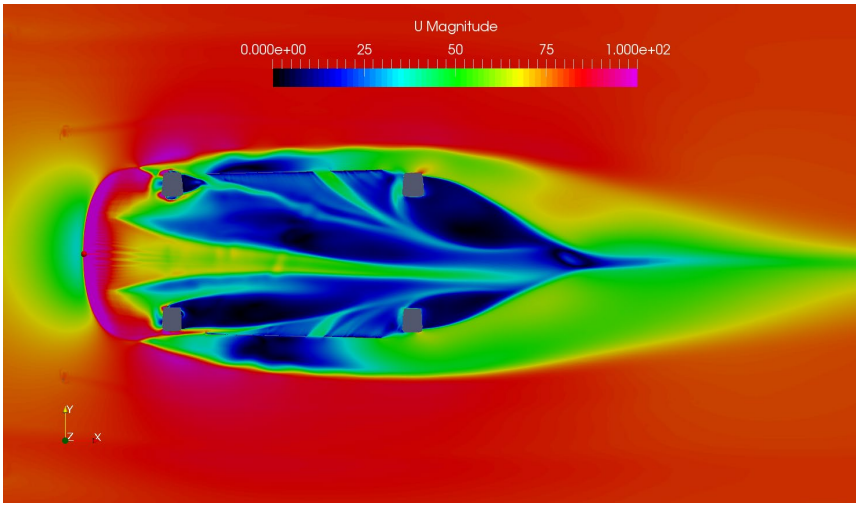

FIGURE 29: Center jet under 2016 Toyota Camry at z=h/2.

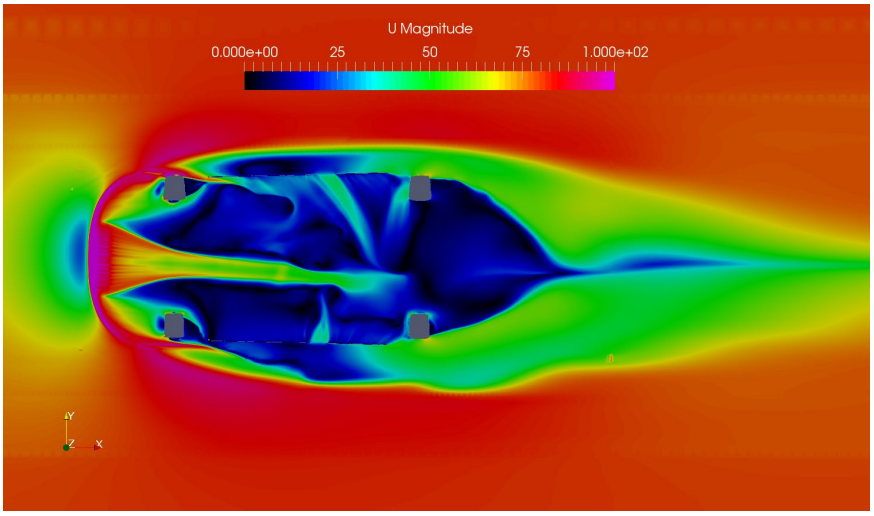

FIGURE 30: Center jet under 2017 Toyota Camry at z=h/2.

Flow from splitter side wings feeds the center jet and keeps it from dissipating. Larger side wings on the 2016 splitter are able to keep center jet energized longer. FIGURE 31 compares jet centerline velocities for both cars.

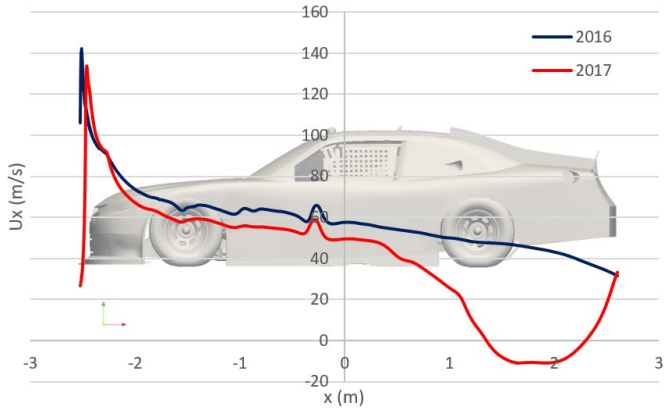

FIGURE 31: Jet centerline x-velocity at z=h/2.

Zero x-location is positioned at the center of the car. Negative values of the x-axis are towards the front of the car and positive – towards the rear of the car. According to FIGURE 31, both jets have similar centerline velocity magnitude under the splitter. 2016 car has slightly higher velocity under the engine after flow leaves the splitter when compared to the 2017 jet centerline velocity. Higher flow velocity correlates well with lower pressure measurements from probes 1 and 2 on FIGURE 23. Finally, center jet dissipates completely under the 2017 car, about 1.3m downstream from the center of the vehicle, which results in the increase in pressure measurements from probes 7 and 8.

All in all, most of down-force change came from reduction of splitter surface. There is less area that can capture pressure difference between top and bottom of the splitter. Most of the drag reduction came from spoiler size reduction. Less down-force decreases cornering speed while less drag increases straightaway speed. This means that cars will be faster on the straight and slower in the corner. Overall effect on vehicle lap speed is shown on FIGURE 32.

Not all race track from a race season are represented on FIGURE 32. Daytona International Speedway, Talladega Superspeedway, and Indianapolis Motor Speedway were removed from comparison as different aerodynamic rules apply for these tracks.

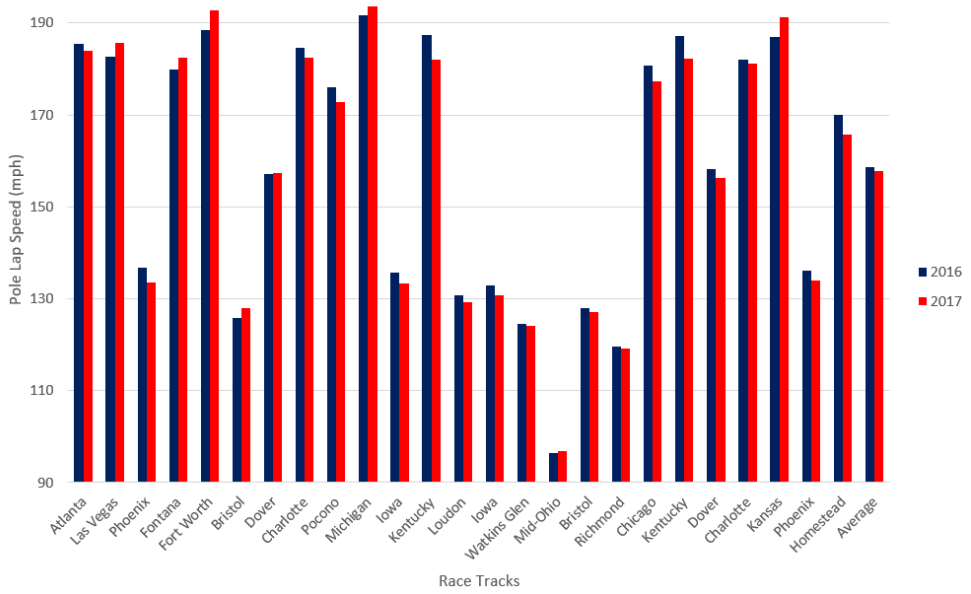

FIGURE 32: Pole lap speed by track.

Track at Fort Worth Texas was resurfaced before the beginning of 2017 season and for this reason was not included in comparison. Bristol 1 was also excluded because traction compound was added to race track surface in 2017 season. Other races were not accounted because ether in 2016 or in 2017 season qualification was canceled. Weather can have an effect on lap speed, that is why it is hard to compare lap speed for different packages individually from track to track. For this reason, it is more reasonable to compare average pole lap speed. After introduction of 2017 aerodynamic rules cars on average went 1.225 mph slower a lap. This proves importance of down-force for race vehicle performance.

CHAPTER 5: CONCLUSION

Because OpenFOAM is an open source software, it allows to conduct unlimited tailoring for specific needs. With its help I was able to create complicated meshes and perform simulation of turbulent flow around NASCAR Xfinity racing series stock car. The mesh sensitivity study was performed to make sure mesh did not skew the final results. Additionally, a modification of turbulence model coefficients was needed to improve correlation of the flow field with wind tunnel results. Simulations were performed at two different ride heights. RH1 is a vehicle ride height that resulted in lower drag and is appropriate for faster tracks. RH2 is a vehicle ride height that resulted in higher down-force numbers. Despite such a dramatic vehicle attitude changes, CFD was able to keep correlation to wind tunnel results. This fact gave me confidence that comparing two different aerodynamic packages would be accurate from a simulation point of view.

Introduction of the new aerodynamic rules for 2017 racing season resulted in significant loss of down-force and drag. Most of the drag decrease came from the rear spoiler reduction. Because the spoiler became shorter, less air was trapped on front of it. Lower pressures pushed on the top of the rear deck lid, which resulted in small rear down-force decrease. Most of down-force reduction was obtained by reducing front splitter size. Smaller splitter on 2017 cars radically changed under-body flow. Center jet lost its strength, which on average increased pressure under the car.

Simulations correlate well with down-force and side-force measurements from wind tunnel. There is great discrepancy in drag correlation. Additional study is required to improve drag prediction by CFD. On the other hand, simulation was able to accurately

predict drag change between different aerodynamic rule packages along with other force coefficients. In order to improve correlation, an array of pressure probes is required to measure the flow field during wind tunnel test. This will allow to study in detail the discrepancies between CFD and experimental results. Flow filed measurements will provide data that can be used to modify turbulence model along with boundary conditions.

Lower drag coefficient allows cars to accelerate faster on straights, but drivers have to slow down more because of down-force reduction, which puts more stress on braking system. At the same time noticeable increase in racing quality has not been observed. Moreover, for 2019 NASCAR Monster Energy Cup series it was decided to go back to high down-force and high drag package in an attempt to increase competitiveness. As for NASCAR Xfinity racing series rules stayed unchanged as of 2019 season.

REFERENCES

Catranis, D. (2018). Correlation of Cloud Based Computational Fluid Dynamics Simulations to Wind Tunnel Test Results for a NASCAR XFINITY Series Vehicle.

Collin, C., Indinger, T., & Müller, J. (2017). Moving ground simulation for high performance race cars in an automotive wind tunnel. *International Journal of Automotive Engineering*, *8*(1), 15-21.

Fu, C., Bounds, C., Uddin, M., & Selent, C. (2019). *Fine Tuning the SST k− ω Turbulence Model Closure Coefficients for Improved NASCAR Cup Racecar Aerodynamic Predictions* (No. 2019-01-0641). SAE Technical Paper.

Fu, C., Bounds, C. P., Selent, C., & Uddin, M. (2019). Turbulence modeling effects on the aerodynamic characterizations of a NASCAR Generation 6 racecar subject to yaw and pitch changes. *Proceedings of the Institution of Mechanical Engineers, Part D: Journal of Automobile Engineering*, 0954407019826475.

Fu, C., Uddin, M., & Robinson, A. C. (2018). Turbulence modeling effects on the CFD predictions of flow over a NASCAR Gen 6 racecar. *Journal of Wind Engineering and Industrial Aerodynamics*, *176*, 98-111.

Fu, C., Uddin, M., Robinson, C., Guzman, A., & Bailey, D. (2017). Turbulence models and model closure coefficients sensitivity of NASCAR Racecar RANS CFD aerodynamic predictions. *SAE International Journal of Passenger Cars-Mechanical Systems*, *10*(2017-01-1547), 330-344.

Fu, C., Uddin, M., & Selent, C. (2018). *The Effect of Inlet Turbulence Specifications on the RANS CFD Predictions of a NASCAR Gen-6 Racecar* (No. 2018-01-0736). SAE Technical Paper.

Jacuzzi, E., Aleman Chona, M., & Granlund, K. O. (2019). Improvements in NASCAR Race Vehicle Side Force and Yawing Moment Stability in Race Conditions Using Active or Passive Blowing. In *AIAA Scitech 2019 Forum* (p. 0592).

Jacuzzi, E., Barrier, A., & Granlund, K. O. (2018). NASCAR Race Vehicle Wake Modification via Passive Blown Ducts and its Effect on Trailing Vehicle Drag. In *2018 AIAA Aerospace Sciences Meeting* (p. 0558).

Jacuzzi, E., Granlund, K. O. (2018). Yaw Moment Modification in NASCAR Race Vehicles via Passive Tail Blowing. In *2018 Flow Control Conference* (p. 3529).

Jenckes, C. H. (2016). The Simulation of Road vehicles in Ground Effect.

Lienhart, H., Becker, S. (2003). Flow and turbulence structure in the wake of a simplified car model. *SAE transactions*, 785-796.

Menter, F. R. (1994). Two-equation eddy-viscosity turbulence models for engineering applications. *AIAA journal*, *32*(8), 1598-1605.

Menter, F. R. (2009). Review of the shear-stress transport turbulence model experience from an industrial perspective. *International journal of computational fluid dynamics*, *23*(4), 305-316.

Menter, F. R., Kuntz, M., & Langtry, R. (2003). Ten years of industrial experience with the SST turbulence model. *Turbulence, heat and mass transfer*, *4*(1), 625-632.

Singh, R. (2008). *CFD simulation of NASCAR racing car aerodynamics* (No. 2008-01-0659). SAE Technical Paper.

Sodja, J. (2007). Turbulence models in CFD. *University of Ljubljana*, 1-18.

Tunay, T., Yaniktepe, B., & Sahin, B. (2016). Computational and experimental investigations of the vortical flow structures in the near wake region downstream of the Ahmed vehicle model. *Journal of Wind Engineering and Industrial Aerodynamics*, *159*, 48-64.

Uddin, M., Mallapragada, S., & Misar, A. (2018). *Computational Investigations on the Aerodynamics of a Generic Car Model in Proximity to a Side-Wall* (No. 2018-01-0704). SAE Technical Paper.

Wilcox, D. C. (1998). *Turbulence modeling for CFD* (Vol. 2, pp. 172-180). La Canada, CA: DCW industries.